Structures 50 (2023) 494–507

Contents lists available at ScienceDirect

Structures

journal homepage: www.elsevier.com/locate/structures

ASR crack identification in bridges using deep learning and texture analysis

Andy Nguyen [a,*], Vahidreza Gharehbaghi [b], Ngoc Thach Le [c], Lucinda Sterling [d], Umar Inayat Chaudhry [e], Shane Crawford [f]

[a] School of Engineering, University of Southern Queensland, Queensland, Australia
[b] Department of Civil Engineering, University of Kansas, Lawrence, USA
[c] Department of Hydraulic Engineering, Hanoi University of Civil Engineering, Hanoi, Vietnam
[d] Harrison Infrastructure Group, Queensland, Australia
[e] Sultana Research and Development, Queensland, Australia
[f] RoadTek, Department of Transport and Main Roads, Queensland, Australia

ARTICLE INFO

Keywords:
Alkali-Silica Reaction
Structural Health Monitoring
Artificial Intelligence
Deep Learning
Feature Enhancement
Texture Analysis
Two-stage Assessment

ABSTRACT

Alkali-Silica Reaction (ASR), commonly known as 'concrete cancer,' is an expansive reaction occurring over time between aggregate constituents and alkaline hydroxides from cement. As a destructive phenomenon, the need to detect the onset of ASR in concrete structures to ensure their long-term durability and structural integrity is thus evidenced. In the structural health monitoring field, vision-based approaches have been found to be viable, fast, and cost-effective in diagnosing numerous types of cracks using physical attributes and surface patterns. However, achieving high accuracy in detecting ASR cracks using traditional visual inspection techniques is challenging and time-consuming. Inspired by artificial intelligence technology, this paper proposes and evaluates a two-phase computer vision procedure for detecting and classifying ASR cracks utilizing a collection of ASR images recorded from several bridges in Queensland, Australia. In the first phase, the procedure compares common pre-trained CNN models to investigate their capability in classifying ASR cracks and to select the best-performed model. In the second phase, a novel Feature Enhancement Process (FEP) was first proposed to increase the contrast between ASR cracks and the heavily textured backgrounds within the images. Next, to better highlight the ASR crack features, the feature-adjusted images are processed further through different texture analysis algorithms including: (i) Texture Morphology, (ii) Adaptive thresholding, and (iii) Local range filtering. The study shows that the proposed FEP can improve the ASR crack classification accuracy of InceptionV3, which is the best CNN model selected from Phase 1, from 90.9% to 92.48%. Furthermore, by combining FEP with texture morphology, a robust two-stage tool for assessing ASR cracks can be made with an impressive validation accuracy of 94.07%. This research contributes towards the application of novel AI deep learning technology in providing cost-effective autonomous ASR crack classification tools to support the owners and managers of civil public works assets and other constructed infrastructures.

1. Introduction

Concrete is one of the most popular building materials due to its affordability, availability, adaptability to any architectural shape, and resistance to adverse environmental conditions. Despite these advantages, concrete is not immune to deterioration and damage due to a combination of factors such as overloading, rebar corrosion, freeze–thaw deterioration, chemical attack, abrasion/erosion, and restraint to volume changes [18]. These visual and structural effects are more commonly noted in structures exposed to harsh climatic conditions, especially in coastal regions. All these abnormalities could threaten the performance and integrity of important concrete structures such as buildings, bridges, and dams. Therefore, monitoring and detecting abnormal behaviours based on the assessment of physical conditions and structural responses are crucial for ensuring structural serviceability and durability. Toward this end, Structural Health Monitoring (SHM) technology provides several evaluation frameworks for identifying and assessing changes in the material properties and structural geometry, which helps determine structural adequacy.

Visual inspection is a common and initial approach adopted to

* Corresponding author.
E-mail address: andy.nguyen@usq.edu.au (A. Nguyen).

https://doi.org/10.1016/j.istruc.2023.02.042
Received 4 November 2022; Received in revised form 6 February 2023; Accepted 8 February 2023
Available online 17 February 2023

identify the existence of structural damage. While manual inspection requires skilled experts and is expensive and time-consuming, it may also be dangerous in situations where inspectors must climb to high altitudes to assess structures such as dams and high-rise buildings. Furthermore, inspecting an entire area of such large infrastructures in a short period of time is unrealistic.

To overcome these shortcomings, over the last few decades, computer vision-based SHM has emerged as a more practical condition monitoring technique by providing faster, more accurate, and more secure solutions utilizing cameras, image processing techniques, and automated algorithms while minimizing human intervention at the site. Computer vision is the method of reading and interpreting images in a manner analogous to that of the human brain but using pixel readings. The method commonly incorporates image processing techniques to enable object classification, identification, and tracking [5]. Considering the ease of use and low cost of data setup and retrieval, computer vision is becoming increasingly popular in the SHM field [14]. These techniques have been identified as a critical element for the enhancement of the monitoring and inspection in real-world engineering structures, in which images provide visual data in the same way that skilled specialists do through in-field inspections. Due to this similarity, computer-aided structural inspections are predicted to be implemented similarly to human visual inspections. Moreover, such assessments benefit from rapid analysis facilities that decrease the cost and time of inspection through a contactless fashion, thereby alleviating some of the challenges associated with monitoring using contact sensors.

In the realm of structural engineering, significant research has been undertaken on the design and modification of computer vision systems for inspection and monitoring responsibilities. Moreover, when combined with cameras and drones, vision-based technologies provide rapid and automated inspection and monitoring of civil infrastructure in a safer and more economical way [31].

Artificial Intelligence (AI) has permeated practically all engineering applications as a result of rapid advances in computer technology. AI is the automation of cognition in the sense that it can perform cognitive processes that the human brain is capable of, and is constantly evolving [1]. This makes decision-making a critical component of AI capabilities. With recent advances in knowledge and technology, computational processing has become more cost-effective and adaptive, thus increasing the use of AI in the SHM industry. Computational procedures, which have been established as model-based approaches, are becoming an intrinsic aspect of Non-destructive Testing (NDT) within Image Processing Techniques (IPTs), notably for SHM research [2]. AI reliability has a very high potential which can be attributed to two primary subfields: (i) machine learning and (ii) deep learning (Fig. 1).

The first subfield of AI, viz., machine learning, is an automated technique for data processing based on computer models. It is based on structured data that is commonly adjusted by humans through feature extraction [9]. Prior to training a model, feature extraction allows for the classification of multiple data sets. When a model is adequately trained to detect pre-classified categories of intended recognition, it can recognize highlighted sample features independently.

Deep learning is the second branch of AI that incorporates and extends machine learning capabilities in data classification during the preprocessing phase [8]. This is possible because of the use of Artificial Neural Networks (ANN), which may be updated and trained to evaluate and discover the desired object within a dataset for later use [27]. As a result, deep learning is hampered by the need to discover essential traits within the dataset, necessitating the need for a large training set for improved feature detection. As opposed to machine learning, deep learning is capable of hierarchical feature learning.

Within deep learning, a Convolutional Neural Network (CNN) is a type of ANN widely used for image/object recognition and classification. Deep learning thus recognizes objects in an image by using a CNN. A typical CNN architecture starts with convolutional layers that recognize low-level source image characteristics. Therefore, pooling layers collect this new information for use in the following series of convolutional layers that extract higher-level features from the previously examined low-level properties. The data is eventually translated to classification layers, where labelled output prediction happens after this operation is repeated for the depth and breadth of the CNN's architecture [20]. Learning capability is based on the quantity of accessible data for extracting various features to improve learning capability in this connection.

Computer vision based SHM is commonly seen as cost-effective, fast, and not requiring professional expertise. As a result, vision-based surface inspection has been a research focus for decades, particularly for concrete structures. Classical image processing techniques based on manual threshold and heuristic feature-extraction methods or automated deep learning-based approaches, have been used to handle

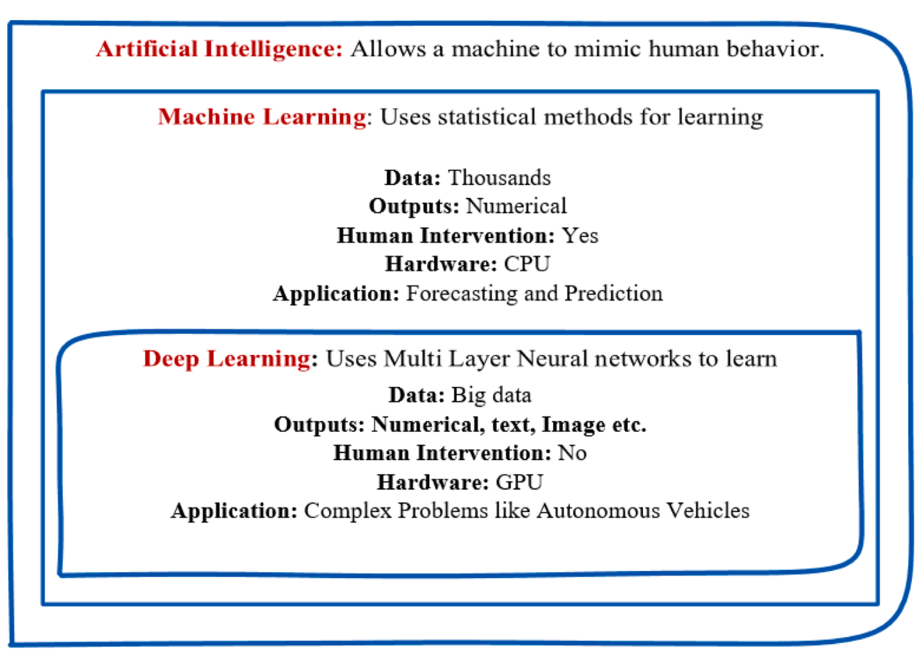

Fig. 1. Artificial Intelligence and Its Subfields.

delamination, spalling inspection, and detection of various concrete cracks.

Alkali-Silica Reaction (ASR) is a destructive phenomenon that causes concrete to crack and degrade. It occurs when concrete is formed using specific alkali-reactive aggregates. ASR in concrete causes internal swelling and micro cracking, which leads to concrete expansion and degradation. While various SHM solutions have been studied for the evaluation of ASR cracks, such as acoustic emission [13,32], microscopic methods [36], and Raman microscopy [21], limited studies are conducted on the classification of ASR cracks using deep learning. There has been no similar research on performance assessment of pre-trained deep learning models, which are common in image classification and refining for ASR crack detection.

We have begun a research project using AI computer vision technology to develop the very first affordable method for assessing ASR damage. Our method is designed to support the owners of civil public works assets through different phases. The present paper focuses on the first phase, which is the automated identification of ASR crack presence through image classification. The following sections will provide a brief history of ASR, including causes, impacts, and visual indicators on concrete surfaces. The image dataset generated from several bridges damaged by ASR is then shown. From there, classical crack classification is used with pre-trained deep-learning models. Next, a novel strategy for enhancing deep learning model refinement and crack classification accuracy is explored. Following the discussion of the results, the conclusion section highlights key findings from this study that can be implemented in future research on computer vision-based ASR evaluations.

2. Background on ASR causes and effects

Alkali-Aggregate Reactivity or AAR, a chemical reaction between certain mineral phases in aggregates and alkali hydroxides in the concrete pore solution, is one of the most damaging distress mechanisms affecting the lifespan of concrete structures worldwide. The most common kind of AAR in concrete is ASR, whereas the Alkali-Carbonate Reaction (ACR) is a less common type. When structures come into direct contact with water and humidity in the air, chemical processes in the concrete particles impair their performance over time. ASR is formed when reactive siliceous aggregate particles in the pore solution of concrete structures combine with hydroxyl ions. When exposed to moisture, the reaction produces a gelatinous fluid that swells and breaks concrete buildings. Minerals with no long-range atomic order, such as acidic volcanic glass and chert, as well as minerals that have lost their initial hierarchical molecular structure, such as strained quartz, are frequent sources of reactive silica. The release of alkali ions (potassium and sodium) during the hydration of Portland cement causes the high concentration of hydroxyls (high pH value) present in the pore solution of Portland cement concrete. As a result, the gel is frequently amorphous and made up of silicon, alkaline water, and calcium. For ASR to be dangerous, the following three conditions must be met [28,37]:

- Reactive siliceous aggregate.
- High alkali content in Portland cement as a resource of high concentration of hydroxyl ions in the pore solution of concrete.
- Existence of moisture (above 75 % relative humidity within the concrete).

This deteriorative chemical reaction is more common in certain areas than others [18]. The extent of reactivity and eventual degradation in any concrete structure can vary greatly depending on the pore solution composition in any given region, specific reactive aggregate particle qualities, and the structural design. The composition and quality (permeability) of the concrete are the most critical criteria for determining the potential severity of ASR. In addition, exposure conditions such as temperature, humidity, drying and wetting, freezing and thawing, and structural restrictions are all elements that influence ASR.

The ASR can severely damage the mechanical properties of concrete, therefore, it is important to detect the onset of an ASR occurrence and monitor its propagation on the structure [26]. Although ASR is a difficult engineering problem, it provides visual cues that aid in diagnosis. The most common visual symptoms of ASR consist of concrete cracking, expansion (causing deformation, relative movement, and displacement of structural members), surface pop-outs, surface discoloration, and gel exudations. A comprehensive description of the symptoms can be found in Thomas et al. [34] and Thomas et al. [33]. Among these visual indicators, concrete cracking is the most common defect, which manifests into two different types depending on the nature of the concrete structures. The classic type of ASR crack is map cracking, which takes the form of randomly oriented cracks on the surface of concrete elements that are relatively free (unrestrained) to expand in all directions (Fig. 2 (a)). Conversely, when expansion is restrained in one or more directions due to internal confinement (rebars or prestressed tendons), or by external forces from abutments or adjacent structures, dominant expansion occurs in the direction of least confinement, and thus forms the second type of ASR crack known as longitudinal or aligned cracking. For bridge girders, ASR cracks usually be aligned horizontally due to the confinement imposed by rebars and/or prestressing tendons parallel to the beam axis (Fig. 2 (b)). Similarly, ASR cracks tend to be aligned vertically due to the restraint imposed by primary reinforcement and the dead load in reinforced concrete bridge piers and columns (Fig. 2 (c)).

With ASR defects, it is highly unlikely to have all the above visual symptoms in one place, yet an individual symptom does not necessarily indicate ASR defects in many cases [33]. For instance, map cracking can also be caused by drying shrinkage and freeze/thaw cycles, creating a pattern of cracks with random orientation. In addition, longitudinal cracks can be caused by reinforcement corrosion. However, research by Fanijo et al. [12] shown that, for structures located in an environment with a renewable source of moisture, clear visual evidence of gel exudations and surface discoloration on map or longitudinal cracks indicates a high probability of ASR presence. This provides an important indicator for visual identification of ASR presence in suspected structures during routine inspection programs.

Visual inspection by specialists is a common way of assessing ASR in such inspection programs. The Lake Lynn project, for example, is a 305-meter-long and 38-meter-tall concrete gravity dam. Nobody had ever heard of AAR before 2004. During a visual inspection in 2007, cracks and spalls were discovered in the deck's expansion joints. Because the expansion joints were filled with dirt, they had no capability for AAR or thermal expansions. However, visual inspection is not cost-effective because it necessitates the training of a large number of professionals to conduct inspections on complex and large structures such as bridges and dams [26].

With the advances in machine learning, researchers have provided new approaches for the prediction of ASR. Oey et al. [24] found that using an "extra trees" type random forest algorithm, an accuracy of 78 % could be achieved when classifying concrete by AAR gel abundance. This accuracy was improved to 82 % when applied to the simpler classification of the existence (or not) of AAR gel in the concretes and to 90 % when factoring in the relatively lower "cost" of falsely predicting the occurrence of AAR. Allahyari et al. [4] used ANN and chemo-mechanical and kinetics-based approaches to develop a time-and-temperature-dependent model of ASR. A comparison between the developed model and a chemo-mechanical one showed higher accuracy for the developed model.

Deep learning algorithms have been applied for the evaluation of ASR defects by researchers. For example, Ai et al. [3] used Acoustic Emission (AE) to validate the performance of two deep learning models in the ASR detection of a concrete specimen. To that purpose, AE signals were employed to record stress from concrete surfaces in the presence of ASR. The expansions were measured on a regular basis with strain-mounted gages. Two deep learning algorithms, a CNN and a stacked

Fig. 2. (a) ASR map cracking, (b) ASR longitudinal cracks in bridge girder, (c) ASR longitudinal cracks in bridge columns [34].

autoencoder, were utilized to classify structural conditions into two classes using AE data and to determine ASR volumetric using recorded strains. The results demonstrated that CNN outperformed the autoencoder network in terms of accuracy.

ASR-affected reinforced concrete slabs were subjected to moving wheel loading in a study by Adel et al. (2021). Image analysis was used to capture images and assess deflection. They developed the U-Net model to identify pit formation along ASR cracks.

In research by Uwanuakwa et al. [35], a deep learning algorithm was used to classify ASR concrete images from the public repository. The images were analysed using the visual geometry group (Vgg19), neural search architecture (Nasnetlarge), and residual inception block (vinceptionresnetv2) algorithms. The overall performance results indicate that the Vgg19 algorithm outperformed the Nasnetlarge and Inceptionresnetv2 algorithms in identifying and classifying concrete cracks.

Bezerra [7] developed a CNN-based method for predicting the Damage Rating Index (DRI) to automate the DRI test methodology for measuring the degree of concrete damage caused by ASR. This procedure consisted of two steps: crack recognition utilizing sliding windows and enhanced pixel recognition. The DRI number estimation was then applied to the CNN model with an accuracy of 74.4 %.

With the above literature review, there is a need for an automated ASR evaluation tool that can monitor huge structures while remaining cost-effective, fast enough, and accessible to all engineers. The answer is provided by computer vision, which employs automated algorithms based on deep learning and monitors large areas using drones and other digital cameras. The following section illustrates the details of the image dataset used in this paper.

3. Creation of an image dataset for ASR crack identification

To create an ASR image dataset, some real bridges affected by ASR were investigated as case studies. Since ASR normally takes time to form and the focus of acquired images is on ASR damaged bridges, this dataset is valuable for future computer vision-based investigations in the realm of SHM. A total of 35 original images of areas subject to ASR used in this study were taken as part of periodic inspections from several bridges in Queensland, Australia over the course of many years. The images creating the dataset for this research were retrieved with permission from the Bridge Information System (BIS) at Queensland's Department of Transport and Main Roads (TMR). Some of the image samples are presented in Fig. 3.

All the examined bridges are in the locations subjected to renewable source of moisture. Visual inspections conducted by TMR identified longitudinal cracks along the girders, clearly visible with gel exudations and surface discoloration (Fig. 3 and Fig. 4). These indicators have helped to detect the presence of ASR defects in the bridges according to the common visual symptoms of ASR presented in Section 2.

Fig. 3. Image Samples from Queensland Bridges.

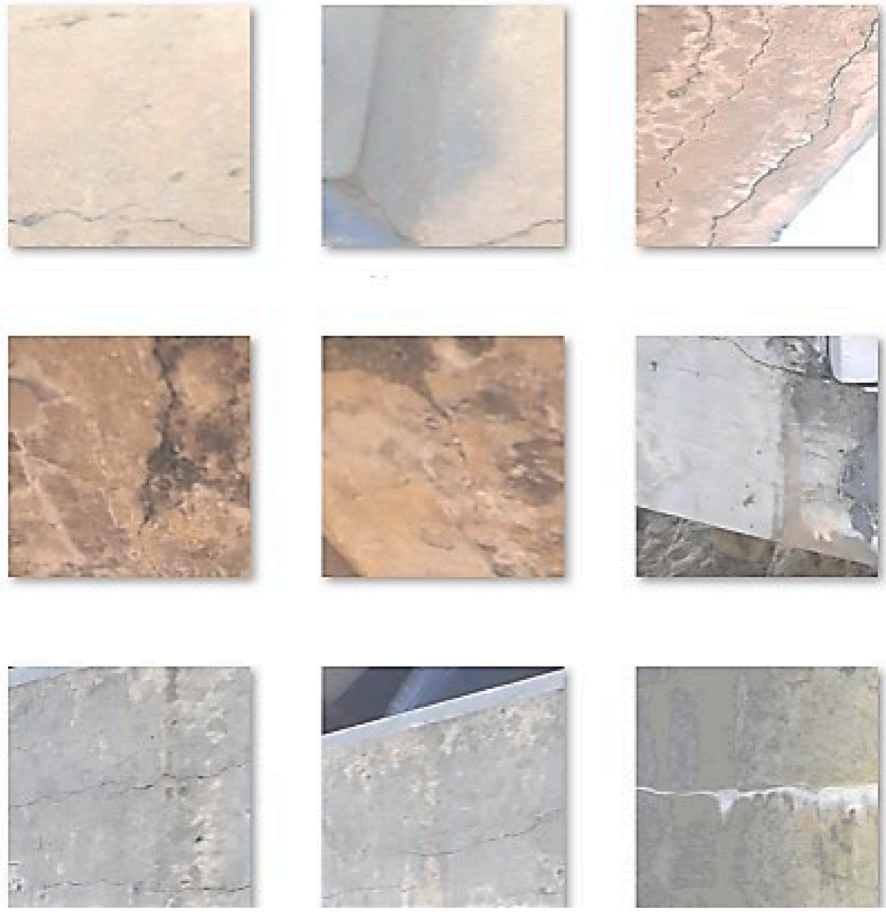

Fig. 4. Samples of ASR Cropped Images from The Original Dataset.

The batch of images extracted from the BIS at TMR contained various resolutions and dimensions. All of the image dimensions indicated in this dataset were much greater than the CNN input dimension requirements, which can degrade image resolution. In order to preserve image resolution, image cropping must occur, similar to the pre-processing method developed by Silva and Lucena [29]. In addition, previous studies indicate that a large training dataset is necessary for effective CNN training [8]; hence this cropping approach preserves image resolution while providing a substantially larger training dataset.

Silva and Lucena [29] and Cha et al. [10] adopt 256 × 256 image pixels for training, which creates a small enough patch size to have a negligible impact on resolution quality when automatic resizing occurs during input [22]. By adopting a 256 × 256-sized image patch, an automated image cropping script has been created for this study. The 256 × 256 image patches obtained through this process shall thus form the image dataset.

CNN training for this project required a subset of images that contained cracks and an additional subset containing no cracks. Images containing no features representing a crack adopted a naming convention of the base. Thus, this research observed a binary format. This enables the CNN to detect ASR defects using the cracked dataset as well as non-crack images from the base dataset. To create these two subsets, manual identification and selection of each image patch are generated by the cropping process and afterward transferred to the respective subset category folder.

In conclusion, from the image pre-processing phase, the dataset contained 1097 base images and 609 ASR defect images from Queensland bridges at 256 × 256 patch size, summing to 1706 images in total for the dataset hereafter called original, or raw dataset. Fig. 4 shows some of the image samples from the dataset created after cropping.

4. Phase 1 of ASR crack Identification: Sole use of Pre-trained models

4.1. Selection of Pre-Trained deep learning models

As previously mentioned, pre-trained deep learning models are very popular for image classification in numerous engineering and medical applications due to their rapid performance, simple training, and straightforward deployment with the new datasets. Thus, in the first phase of this study, we employ some traditional pre-trained models to investigate their capability in classifying ASR cracks. This phase aims to determine which pre-trained models perform best with the ASR defect dataset. The most suitable models for consideration are selected following recommendations from Nguyen et al. [23], who conducted a comprehensive analysis of the performance of eight common deep neural networks in the context of automated crack identification under normal and unfavourable environmental circumstances by investigating variety of criteria, including batch size, model size, and the number of runs. Consequently, three models, namely ResNet-18, InceptionV3, and AlexNet, are selected in this study. The first model (ResNet-18) is selected due to its excellent performance in the trade-off between classification accuracy and computational cost, while the second model (InceptionV3) is selected owing to its robustness against image noises, such as motion blurs and Salt and Pepper noise, which are commonly induced in images taken from real structures. The last model (AlexNet), which is reportedly less robust than the other two counterparts [23], is selected herein owing to its advantage in computational cost since it processes through only eight layers (compared to 18 and 48 layers for the Resnet18 and InceptionV3, respectively). The CNN architectural details of the three selected networks are provided in Table 1 below.

Using knowledge gained from the literature, each pre-trained CNN should be adapted for transfer learning [16]. When each CNN was modified for transfer learning, the generic pre-trained architecture was imported. To enable transfer learning, the last layer in the network, i.e., the classification layer, was deleted and replaced by a new classification layer with the output size set to 'auto'. Similarly, the final fully connected layer in the network was deleted and replaced by a new fully connected layer with the output size set to 2, meaning one output for base classification and another output for ASR defect.

4.2. Pre-Trained CNN performance evaluation criteria

In order to evaluate the efficiency of the pre-trained models in classifying ASR cracks, the following common performance indices for CNN are employed in this study: (1) F1-score, (2) Model overfitting, and (3) Validation accuracy.

In statistical analysis of binary classification, the F1-score, which ranges from 0 (unable to classify) to 1 (perfect classification), is a measure of accuracy within a model which combines other performance indices, namely "precision" and "recall" as depicted in the following equation:

$$\text{F1 score} = \frac{2 \times \text{Precision} \times \text{Recall}}{\text{Precision} + \text{Recall}} \tag{1}$$

Where, Precision (also called positive predictive value) is the fraction of relevant instances among the retrieved instances, while Recall (also known as sensitivity) is the fraction of relevant instances that were retrieved, which can be expressed as follows:

$$\text{Precision} = \frac{\text{No. True positives}}{\text{No. True positives} + \text{No. False positives}} \tag{2}$$

$$\text{Recall} = \frac{\text{No. True Positives}}{\text{No. True positives} + \text{No. False degatives}} \tag{3}$$

It is evidenced from Eq. (1) that F1-score harmonizes precision and recall indices and provides a convenient performance measure for network comparison, and hence is employed in this study as a unique criterion for comparing the performance of the deep learning models.

Model overfitting is another indicator that commonly used to evaluate the accuracy of CNN models. Overfitting occurs when model generalization does not transfer from training data to unseen data, i.e., the training data is learned well, however, the model does not generalize this information well for use on new information. Overfitting is apparent when training accuracy and validation accuracy are not cohesive.

4.3. Pre-trained CNN performance evaluation results

Testing of the selected networks occurred firstly with controlled (or default) training parameters, followed by a second run incorporating data augmentation, reduced initial learning rate, and reduced mini-batch size to demonstrate improvement in CNN performance. It should be noted that throughout this research, the training–testing trials for each investigation were carried out at least 10 to 15 times to exclude the outliers and derive an average validation accuracy rate within a maximum standard deviation of 1 %.

The image classification results are shown for each deep learning model. First, the models were tuned in terms of hyperparameters to reach the highest accuracy. Hyperparameters are the initial settings that control the behaviour of the model and adjust the learning process. Choosing fitting parameters plays a crucial role in achieving the accuracy and convergence of a deep learning network. The learning rate, number of epochs, and batch size are among the most common hyperparameters. Although optimizing the hyperparameters is an onerous task, several researchers have investigated the effects of these parameters on different networks. Based on previous research by Nguyen et al. [23], the hyperparameters provided in Table 2 were used as the first trial for the training of the three models. RandRotation in the table denotes the degree of rotation applied to the input image. RandScale rotates images at random angles in the [0, 360] degree range and resizes images at random scale factors in the [0.5, 1] range. In all models, 70 % of the input images were used for training, and 30 % of the data was taken for evaluating the performance of the models. As shown in Fig. 5, the first epochs of the model training were troubled by overfitting issues since the training accuracy and validation accuracy were not cohesive.

Due to the overfitting issues, the second run reduced the initial learn rate and mini-batch size, as well as incorporating data augmentation in terms of random rescaling and random rotation. Training details and training graphs are presented below in Table 3 and Fig. 6, respectively. As depicted, the overfitting problem was solved significantly in the refined model.

A similar procedure was conducted for the two other models to find the best hyperparameters with the least viable verifiable issues. The best hyperparameters for each model, post-tuning, are summarized in Table 4. As can be seen from the table, the best MiniBathSize for all models is 16, and they all have the same InitialLearnRate of 0.001.

Using the tuning parameters in Table 4, the classification results are derived for the three pre-trained models as shown in Fig. 7. It can be observed from the figure that AlexNet is the lowest-performance model with the least accuracy of 85.5 %. This can be explained by the fact that the model has much smaller number of layers (Table 1) and is a simpler network architecture compared to the other two counterparts. This has made it difficult for AlexNet to extract low-level features related to tiny cracks. RestNet18 offers better performance than the AlexNet, with an accuracy rate of nearly 88.0 %. However, the best-performed model is InceptionV3, with a classification accuracy of over 90.0 %. InceptionV3 is therefore selected to incorporate with image processing techniques to improve the classification accuracy for the ASR crack dataset in the second phase of this study.

5. Phase 2 of ASR crack Identification: Refinement using IPTs

In this phase, a novel image enhancement method is introduced to improve the accuracy of ASR crack classification using the InceptionV3 model selected from Phase 1. The proposed algorithm comprises of two components. First, an innovative feature enhancement method is developed to adjust the images, which were taken from real bridge without any surface treatment, to make ASR cracking more apparent by creating greater contrast between the crack and the background of the image. In the second component, the feature adjusted images will then

Table 1
Architecture of Pre-Trained Models Used in This Study.

Network	Number of layers	Size of Model (MB)	Parameters (Millions)	Image Input Size
InceptionV3	48	89	23.9	299-by-299
Resnet18	18	44	11.7	224-by-224
AlexNet	8	227	61.0	227-by-227

Table 2
Training Parameters and Validation Results ResNet-18 Control.

Training Parameters	InitialLearnRate	0.01
	MiniBatchSize	32
Data Augmentation	RandRotation	[0, 0]
	RandScale	[1,1]
Performance Assessment	Validation accuracy	89.84 %
	F1-score	0.8882
	Overfitting	Significant

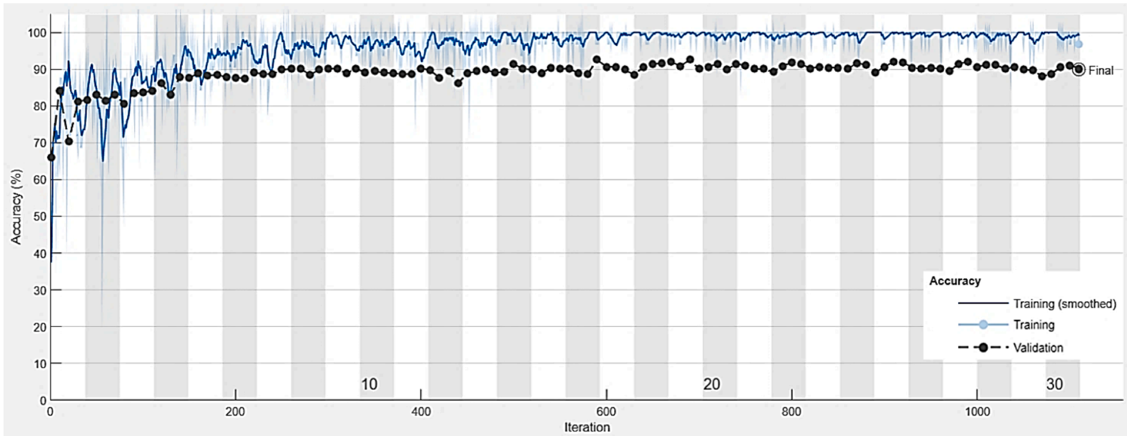

Fig. 5. Training and Validation Plot Examining Overfitting for ResNet-18 Control.

Table 3
Training Parameters and Validation Results ResNet-18 Refined.

Training Parameters	InitialLearnRate	0.001
	MiniBatchSize	16
Data Augmentation	RandRotation	[0, 60]; [0, 180]; [0, 240]; [0, 300]
	RandScale	[1, 1.5]
Performance Assessment	Validation accuracy	87.90 %
	F1-score	0.880
	Overfitting	Negligible

be processed through different texture analysis techniques to further highlight and emphasize ARS cracks from the background existed on the bridge surface. This process will result in new image data subsets for training the InceptionV3 model and for testing its improvement in classifying ASR cracks. The whole process of the proposed method is illustrated in the flowchart in Fig. 8. A detailed description of each step is provided in the following sub-sections.

5.1. Feature enhancement

5.1.1. The proposed feature enhancement process

The first component of the Phase 2 algorithm is a feature enhancement process (FEP) proposed in this study to adjust the original (raw) images (created in section 3). Analysis in this application is carried out through a testing decision tree that evaluates pixel intensities. Since many of the original images were subjected to heavily textured backgrounds, distinctive adjustments, and refinements to create greater contrast of desired ASR crack features from the background are advantageous in reducing CNN evaluation confusion. Rather than working on grayscale images with a single Gray layer as normally seen in existing researches on ASR crack classification, such as in Bajcsy et al. [6], this paper will process through all three RGB layers (Red, Green, and Blue) of the original images. The purpose of this operation is to maintain the colour information of the adjusted images for later texture analysis. A procedure chart for the proposed FEP is presented in Fig. 9.

In the first step of the proposed FEP, all the Base and ASR defect images are scanned to extract the RGB layers. From this extraction, the mean pixel values for each of the three arrays are determined and combined to obtain an average image colour. The three mean pixel values, which represent the average colours of the source image, are then compared to a pre-determined pixel value threshold set at [130 130 130] as approximately a midpoint between true black (i.e., dark) at

Table 4
Tuned Hyperparameters for Pre-Trained Models.

Training Parameters		**RestNet18**	**AlexNet**	**InceptionV3**
	InitialLearnRate	0.001	0.001	0.001
	MiniBatchSize	16	16	16
Data Augmentation	RandRotation	[0,60]; [0,180]; [0,240]; [0,300]		
	RandScale	1,1.5	1,1.5	1,1.5
Performance Assessment	Validation accuracy	87.90 %	85.50 %	90.90 %
	F1-score	0.880	0.854	0.904
	Overfitting	Negligible	Negligible	Negligible

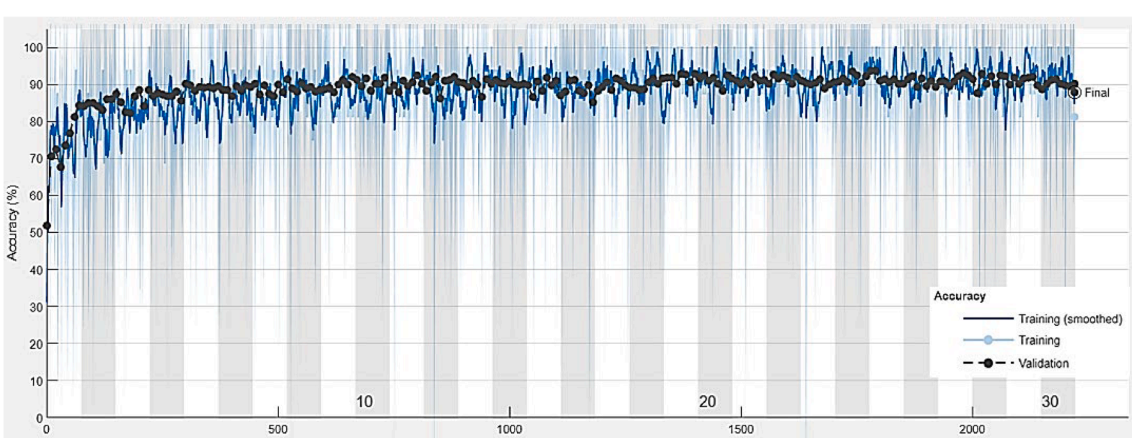

Fig. 6. Training and Validation Plot Examining Overfitting for ResNet-18 Refined.

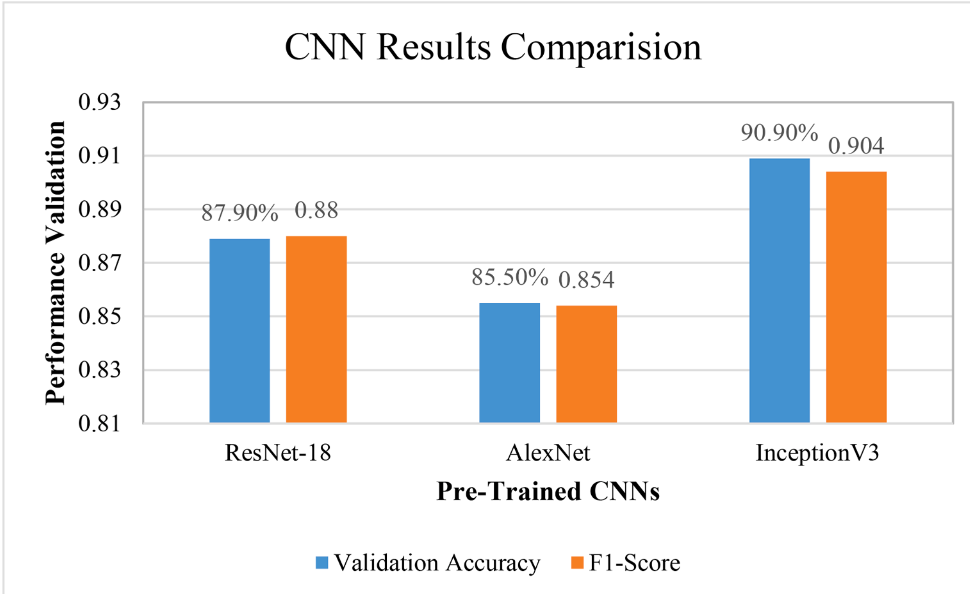

Fig. 7. CNN Validation Accuracy and F1-score Comparison.

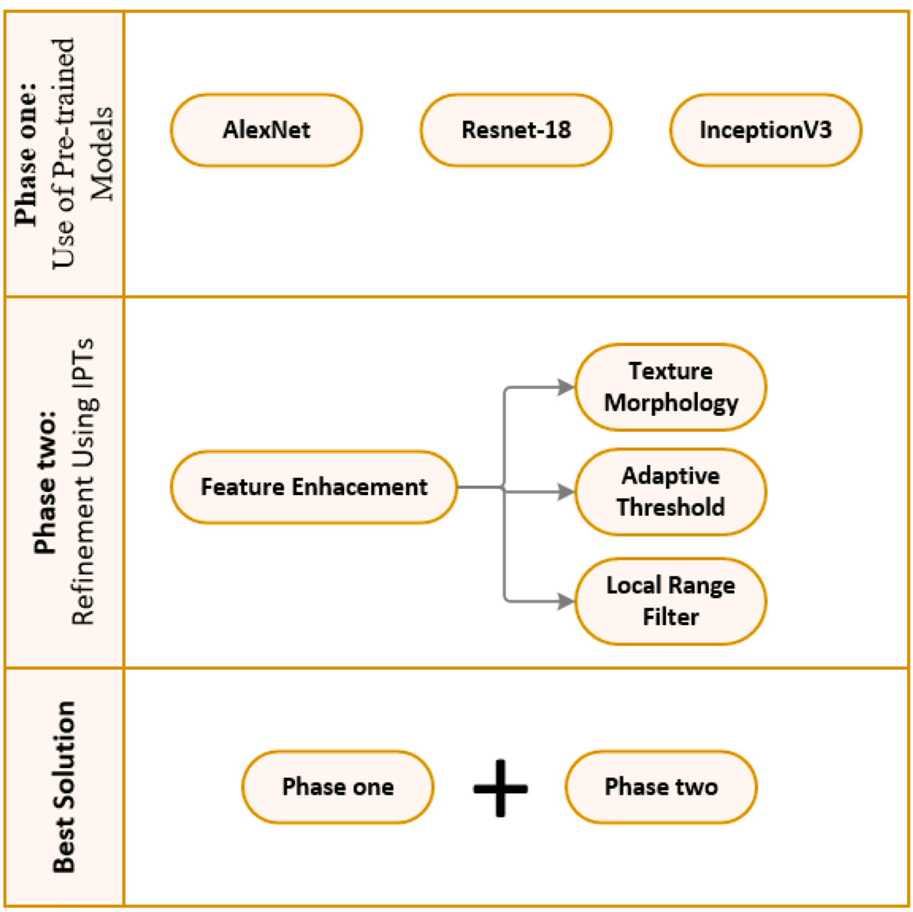

Fig. 8. Research Methodology.

[0 0 0] and true white (i.e., white) at [255 255 255]. If the average value of pixels within the image was less than the threshold, it is generally deemed to be a darker image, whereas, if the average value of pixels is greater than the threshold, the image will be deemed to be a lighter image.

In the second step of the proposed FEP, each image will be targeted once more for each pixel that is darker than a condition dark threshold. Targeting the darker areas of the images aimed to make the ASR cracking more apparent and to create greater contrast between the crack and the background of the image. To create specific measures of light

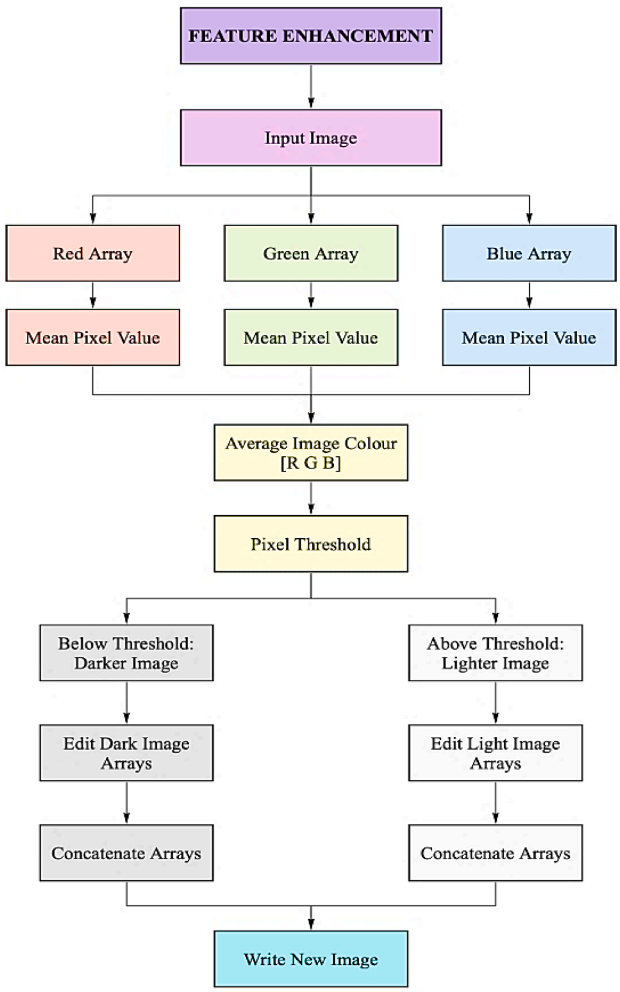

Fig. 9. Feature Enhancement Flow Chart.

and dark pixels, two condition dark values for darker images and lighter images are labelled as follows:

$$Condition\ dark\,(darker\ images) = Threshold - x \tag{4}$$

$$Condition\ dark\,(lighter\ images) = Threshold - x + 50 \tag{5}$$

where, Threshold = 130 is the pre-determined pixel value threshold, x is the feature adjustment value varying from 160 to 60 to ensure that the condition dark value is in the range of [0, 120]. If the image generally reads as darker in nature and a pixel within an array of this image is less than the condition dark, the pixel value will be set to the mean pixel value of that array minus 100. In contrast, if the image is generally lighter in nature and a pixel within an array is less than the condition dark, the pixel value will be set to the mean pixel value of that array minus 50. This process is repeated for all three arrays (R, G, and B). Once completed, the three edited arrays are concatenated to recreate an enhanced version of the original input image.

5.1.2. Finding the best condition dark values

To find the best condition dark values that would yield the highest validation accuracy of ASR image classification, a parametric study is carried out among six feature adjustment values ranging from 160 to 60. Subsequently, six feature enhancement (FE) scenarios were created, and the corresponding condition dark values (for darker images and lighter images) are presented in Table 5. It should be noted that negative condition dark values for FE_160 and FE_150 were set to 0. The table also shows the percentage of images adjusted by the FEP, which reveals that as × decreases, the condition dark increases and, therefore, more images are adjusted by the FEP. For the cases FE_160 ($x = 160$), 17.1 % of Crack images and 5.3 % Base images were adjusted. For the case FE_60 ($x = 60$), nearly 99 % of Crack images and 89.5 % of Base images were adjusted by the proposed FEP.

Fig. 10 illustrates how the proposed FEP modified the images by comparing the original image with the ones created under the FE_150, FE_100, and FE_60 scenarios. The row (C1) shows an example of a clear ASR crack images without significant dark concentrated background, which resulted in unnecessary or almost unrecognizable adjustments for all FE scenarios. By contrast, in the row ($C2$), a typical crack image with bold painting on the background would need to be treated. It shows that FE_150 partly reduced the darkness of the mark at pixels with relatively high dark intensity, while FE_100 adjusted almost the whole area of the mark, and at the same time, slightly increase the darkness of the pixels on the left edge of the image. For FE_60, the darkness of whole painted mark was also reduced, but a large number of pixels on the left edge were made darker, which adversely added more background noise to the image, hence can reduce the validation accuracy. (B1) and (B2) are examples of the Base images with darker pixels arranging at different regions of the image. Depending on the average pixel number of each image, some relatively dark pixels were made lighter in (B1) or darker in (B2). Also, the adjusted regions were larger in FE_60 than in FE_100 and FE_150.Fig. 11.

To evaluate the effectiveness of the six feature enhancement scenarios in improving the classification accuracy, the selected InceptionV3 model from Phase 1 is used in this parametric study. As a result, the validation accuracy values for the six scenarios along with the previously obtained results for original image from Table 4 (without feature enhancement) are summarized in Table 5 and plotted in Fig. 9 for comparison. It is evident that FE_150 presents the best enhancement option with the highest validation accuracy rate of 92.48 %, which is a 1.58 % improvement from the original result of 90.9 %. The FE_160 scenario also performs well with a slightly lower rate of 92.01 % compared to the FE_150 option. In contrast, the feature enhancement scenarios with adjustment values × ranging from 120 to 60 appear to have less improvement, or even deterioration, in the validation accuracy in comparison to the original result. This result is relevant to the level of image adjustment shown in Table 6, with explanation presented in previous paragraph.

From the above parametric investigation, the feature adjustment value × = 150 is selected hereafter for use with the proposed FEP to adjust the images before they are processed further with texture analysis techniques presented in the next section for a better ASR crack

Table 5
Feature Enhancement Scenarios and Results with Different Adjustment Values.

Feature enhancement scenarios	FE_160	**FE_150**	FE_120	FE_100	FE_80	FE_60
Feature adjustment value (x)	160	**150**	120	100	80	60
Condition dark (darker images)	0	**0**	10	30	50	70
Condition dark (lighter images)	20	**30**	60	80	100	120
Percentage of Crack image adjusted	17.1 %	**23.7 %**	58.4 %	77.8 %	92.7 %	98.9 %
Percentage of Base image adjusted	5.3 %	**7.5 %**	28.6 %	53.8 %	74.4 %	89.5 %
Validation accuracy with InceptionV3	92.01 %	**92.48 %**	91.31 %	91.21 %	90.07 %	88.84 %

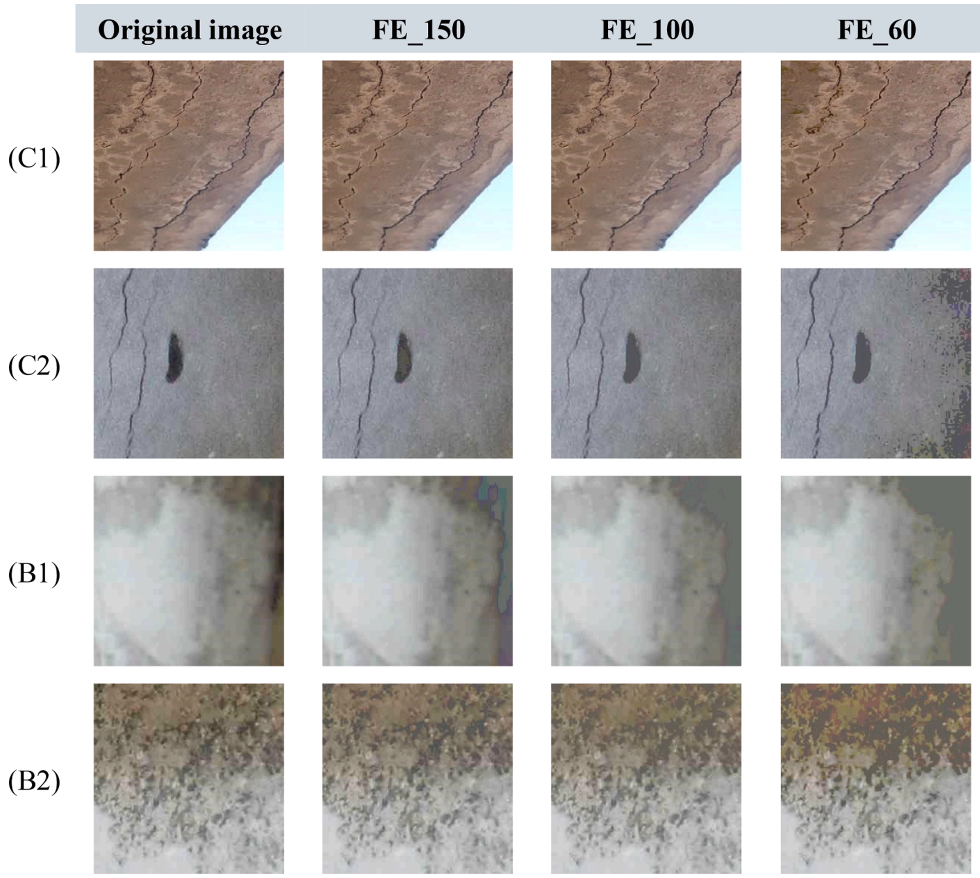

Fig. 10. Effect of FEP on Crack Images (C1, *C*2) and Base Images (B1, B2).

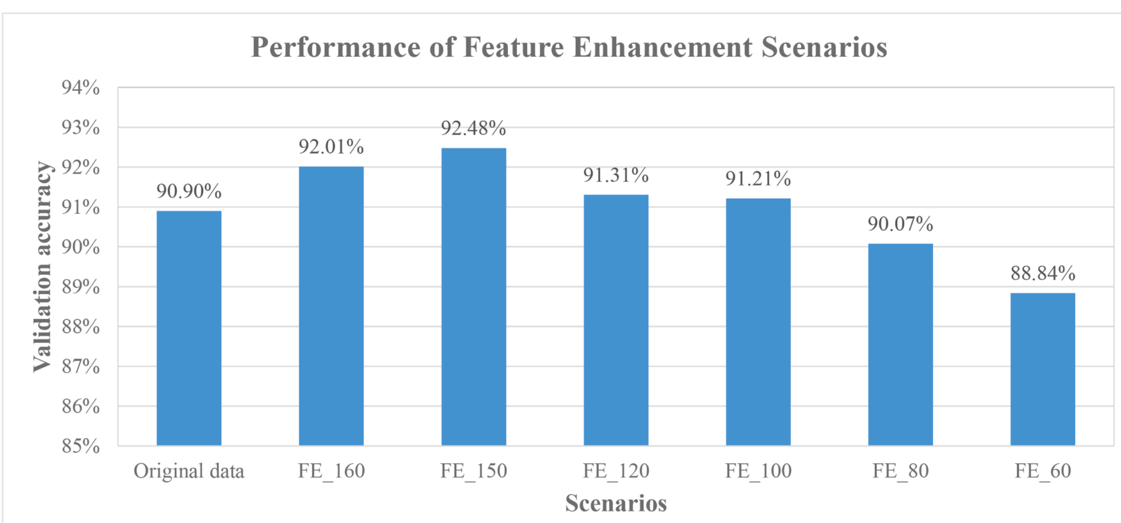

Fig. 11. Performance of Feature Enhancement Scenarios with InceptionV3.

Table 6
Comparison of Texture Analysis Results for InceptionV3.

Performance Assessment criteria	Original	FE_150	FE & Texture Morphology	FE & Local Range Filtering	FE & Adaptive Thresholding
Validation accuracy	90.90 %	92.48	94.07 %	91.23 %	90.37 %
Compared to Original	0 %	1.58 %	3.17 %	0.33 %	−0.53 %
Compared to FE_150	–	0 %	1.59 %	−1.25 %	−2.11 %
F1-score	0.904	0.921	0.937	0.906	0.901
Overfitting	Negligible	Negligible	Negligible	Negligible	Negligible

classification solution.

5.2. Further enhancement with texture analysis

Once the above FEP is completed, the adjusted images will be processed further with texture analysis techniques to find the best solution in Phase 2 of the research methodology highlighted in Fig. 8. Texture analysis can be referred to as the characterization of regions in an image based on their texture content. The technique aims to quantify perceptual qualities such as roughness, smoothness, silkiness, and bumpiness as a function of spatial variation in pixel intensities. In this sense, roughness and bumpiness are the two terms used to describe differences in the intensity values, or pixel values. Numerous texture analysis techniques have been used for image enhancement to make it easier to identify flaws in a visual inspection process. However, it has been evidenced that the use of deep CNN models is superior to traditional image enhancement methods [10,11]. Dorafshan et al. [11] reported that edge detection methods could detect coarse concrete cracks with an accuracy level of 53 % to 79 %, which is relatively low compared to 86 % accuracy when an AlexNet deep CNN model was used. In addition, the crack images used in this study were relatively clear without significant background noise. For heavily textured backgrounds images, such as the ASR defect images in this study, more rigorous texture analyses are required. In this study, three approaches of texture classification techniques, namely Texture Morphology, Local Range Filtering, and Adaptive Thresholding are selected and applied to better highlight the ASR cracks within the images. Details of the three texture analysis methods are briefly outlined in section 5.2.1 below, while the resultant enhanced image subsets are described in section 5.2.2. Finally, the crack identification results from new image subsets using InceptionV3 model are presented and discussed in section 5.2.3.

5.2.1. Texture analysis techniques

a. Texture Morphology.

In mathematical morphology, two-dimensional grayscale images are transformed into different sets by assigning each pixel an elevation that is proportional to its intensity level [17]. It is then used to examine the morphology of the input set, which is referred to as the 'structure element'. Moving the origin of the structural element to every conceivable point in the space and assessing whether the structure is contained inside the studied set or if it has a non-empty intersection within it, is the method used here. For example, by maintaining the inclusion-tested points, one can minimize the input set, whereas the non-empty intersection test causes us to increase it. The two transformations, dilation and erosion, are the fundamentals of morphological operations because all other transformations depend on them. Structuring elements should be chosen according to the morphology of the image structures they intend to target. Line segments, for example, are ideal for evaluating long, elongated systems like fission tracks or fibrous materials, while disks and diamonds are better for analysing small, granular structures [30]. Through preliminary testing, the texture erosion transformation using diamond structuring element are found suitable for making cracks clearer, and hence are selected to use in this study.

b. Local Range Filtering.

The second texture categorization approach used in this study is the local range filtering, which is a common image processing technique dealing with texture background images. Range filtering occurs by taking the minimum pixel value from the maximum pixel value within a set of 3-by-3 neighbourhood around the corresponding pixel in the input image. This technique is helpful in detecting regions of texture in an image and hence can be potential for emphasizing cracks' edges in the ASR images.

c. Adaptive Thresholding.

The third texture classification technique used in this study is adaptive thresholding. The technique divides a digital image according to a specific pixel property (for example, intensity value). Conventional thresholding has been determined to be inferior to adaptive thresholding. Some regions of an image are darker than others, and illuminations can have a considerable impact on the overall appearance of the image. In conventional thresholding, the mean value is derived from a global or standard threshold. If the threshold value is exceeded in an image's darker section, that part will become prominent [25]. If a pixel or pixel fragment goes below this threshold, it is concealed. Adaptive thresholding generates a binary diagram depicting the distinction between threshold levels [19]. Therefore, this technique can be used to highlight cracks from the background of the image.

5.2.2. New image subsets

Fig. 12 illustrates the image processing results for six typical sample patches of the ASR Crack images. The first row of the figure (row (i)) presents the original images. The next three rows present images from three new subsets created by incorporating the FEP with the three texture analysis techniques, which are Texture Morphology in row (ii), Local Range Filtering in row (iii), and Adaptive Thresholding in row (iv). The prefix "FE", which stands for feature enhancement, is added before each texture analysis technique to indicate the combination.

It can be observed from Fig. 12 that the combination of FE & Texture morphology (row (ii)) tends to make the cracks wider and clearer due to the erosion operation. Another advantage of Texture morphology is that it does not change the intensity of background textures (such as painted marks and numbers), which were suitably adjusted earlier through the FEP (3rd and 4th images). Moving on to FE & Local range filter technique, as expected, it helps to emphasize the crack boundaries by increasing their pixel values, while it reduces the pixel values of smooth background, which make the boundaries more obvious. Unfortunately, it also emphasizes the boundary of painted marks, texts, and structural edges. The FE & Adaptive thresholding is also successful in highlighting the cracks, but it also highlights other texture backgrounds, and somewhat make them as clear as the cracks regarding pixel intensity.

Similarly, Fig. 13 illustrates how the three IPTs create three new subsets for Base images in row (ii), (iii) and (iv) from the original image in row (i). The figure shows that FE & Texture morphology tends to slightly enlarge darker regions while keeping the pixel intensity adjusted by FEP. By contrast, the other two IPTs are advantageous in highlighting the textures' boundary where there are significant changes in pixel intensity. However, many of these highlighted texture boundaries (3rd, 4th, and 5th images in Fig. 13) somewhat look like the cracks that they were highlighted in Fig. 12. This can affect the classification results using the two last image subsets.

5.2.3. Performance of feature enhancement incorporating texture analysis

Next, the three enhanced image subsets (each includes a Crack subset and a Base subset) are used separately for training the InceptionV3 model and for testing its improvement in classifying the ASR crack images. Again, the three assessment criteria "validation accuracy", "F1-score", and "Overfitting" are employed to evaluate the performance of IceptionV3.

The subsequent InceptionV3 testing results in conjunction with the three IPTs are presented in Table 6 and Fig. 14 below. Previous results using original images (section 4.3) and feature enhanced images with FE_150 (section 5.1.2) are also included in Table 6 and Fig. 14 for comparison. It is demonstrated that the training processes using all the three image datasets were well-controlled with negligible overfitting. The FE & Texture Morphology solution resulted in a high validation accuracy rate of 94.07 %, which outperforms FE & Local Range Filtering of 91.23 % and FE & Adaptive Thresholding of 90.37 %. The corresponding F1-score also observes a similar trend, which is highest at 0.937 for texture morphology, and much lower at 0.906 for Local Range Filter and 0.901 for Adaptive Thresholding.

In comparison with the original result using raw images, FE & Local Range Filtering indicates a negligible improvement of 0.33 %, while FE

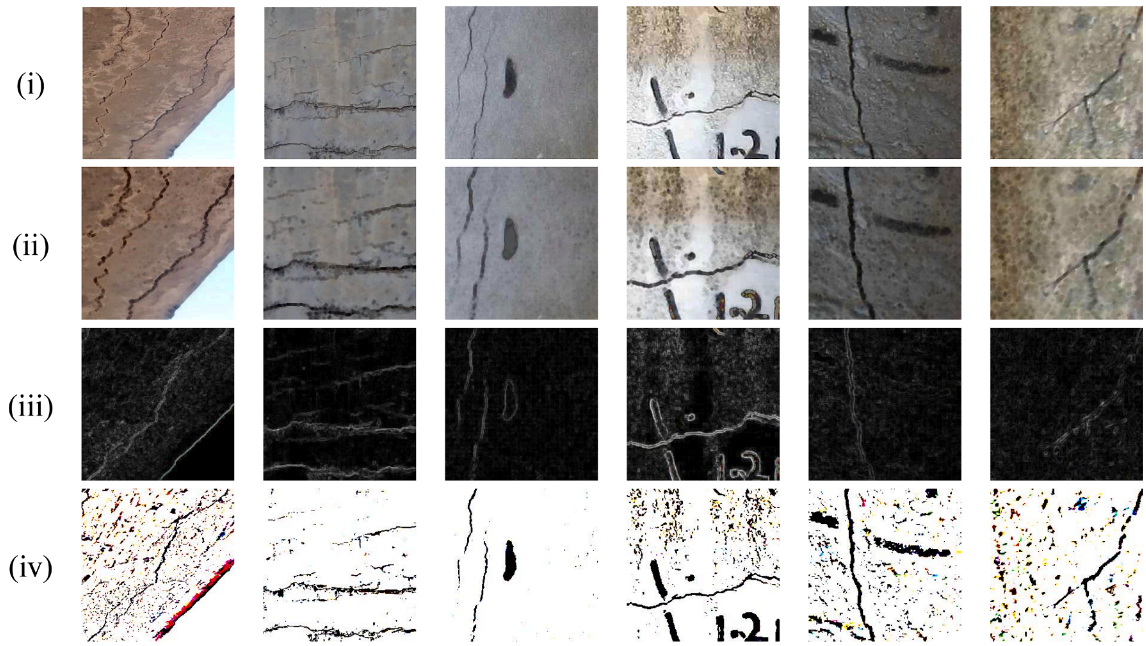

Fig. 12. Examples of Original and New Crack Image Subsets using IPTs: (i) Original, (ii) FE & Texture Morphology, (iii) FE & Local Range Filtering, (iv) FE & Adaptive Thresholding.

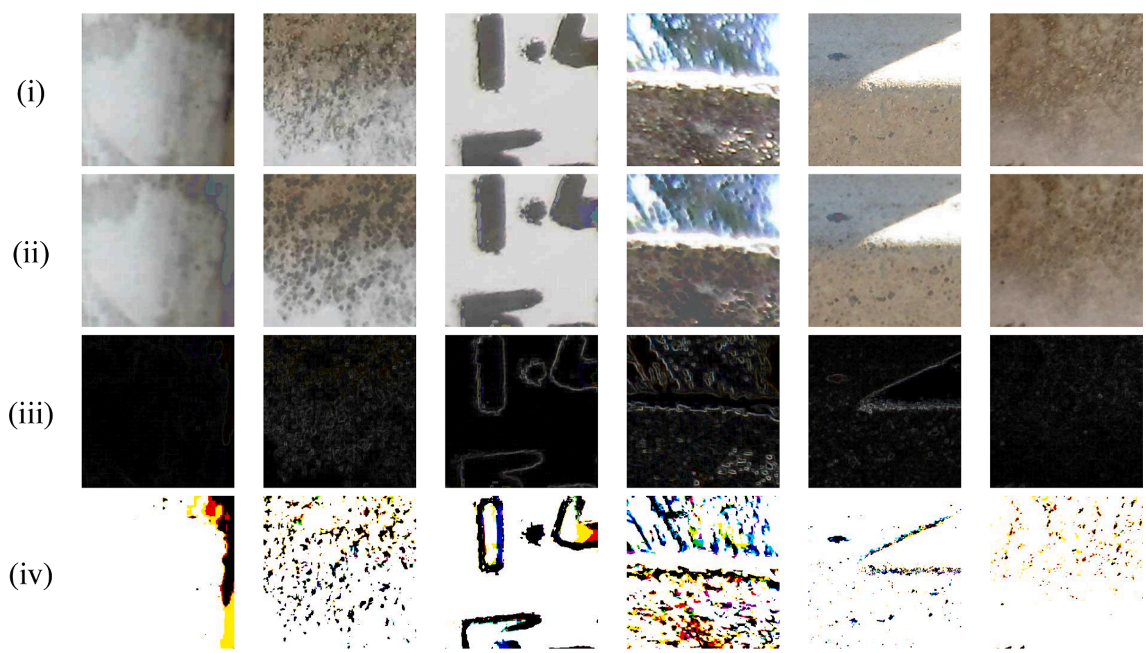

Fig. 13. Examples of Original and New Base Image Subsets using IPTs: (i) Original, (ii) FE & Texture Morphology, (iii) FE & Local Range Filtering, (iv) FE & Adaptive Thresholding.

& Adaptive Thresholding experiences a decrease of 0.53 % in the validation accuracy. By contrast, FE & Texture Morphology presents an increase of 3.17 % in the classification accuracy compared to original result. While this improvement appears small, in the nature of already high results utilising raw data of 90.9 %, there was a significant success in the improvement of ASR crack identification utilising feature enhancement combined with texture morphology.

In addition, it can be seen from Table 6 that Texture morphology, when combined with feature enhancement, can further increase the FE_150 validation accuracy by 1.59 %, from 92.48 % to 94.07 %. Unfortunately, this is not the case for Local Range Filtering and Adaptive Thresholding since these techniques reduce the FE_150 result by 1.25 % and 2.11 %, respectively. This is relevant to what has been discussed on the way the two techniques processed the images in section 5.2.2.

5.3. *Finding best solution*

From the above investigations, it is evidenced that the best approach for the improvement of ASR image classification is by utilising InceptionV3 in conjunction with Feature enhancement combined with Texture morphology. This novel IPT combination approach has proven to be successful in enhancing and sifting out important information of

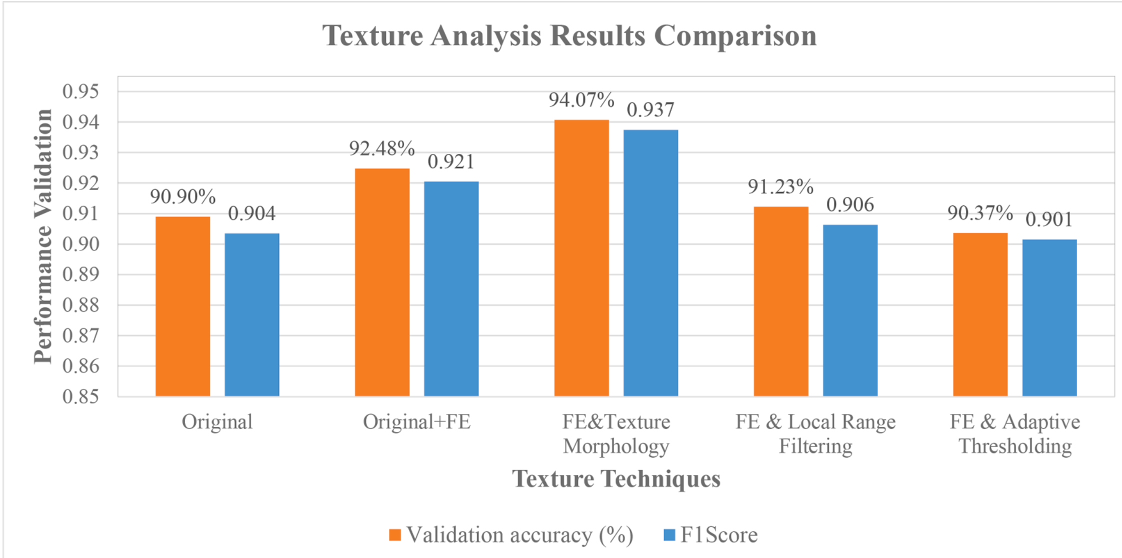

Fig. 14. Performance of InceptionV3 in Conjunction with Image Processing Techniques.

ASR cracks, which has then significantly boosted the performance of the InceptionV3 pre-trained model from 90.9 % to over 94 %. The approach is therefore recommended as the successful two-stage procedure for evaluating ASR cracking powered by AI deep learning technology in this study.

6. Conclusion

This paper developed and presented a novel computer vision-based approach for detecting ASR cracks. The dataset for this research was generated from 35 ASR defect images retrieved from several bridges in Queensland that were impacted by ASR. Cropping raw images resulted in a dataset of 1097 base images (without cracks) and 609 ASR defects images with a 256 by 256 patch size; for a total of 1706 raw images.

Once the benchmark dataset for the ASR crack identification problem is established, a two-stage development is implemented. First, a comprehensive evaluation was carried out to assess the performance of the three common pre-trained CNNs, namely ResNet-18, AlexNet, and InceptionV3, with respect to their training parameters: initial learning rate, mini-batch size, and image data augmentation. It was found that using an initial learning rate of 0.001, a mini-batch size of 16, and the picture data augmentation in the form of random rotation and scaling, the InceptionV3 model responded best with an impressive validation accuracy of 90.90 % in classifying raw ASR defect images.

In the second phase, an enhancement algorithm was proposed to improve the accuracy of the Inception V3 model in detecting ASR cracks using feature enhancement processing incorporating several texture analysis techniques applied to the raw images. To this end, a novel Feature Enhancement Process (FEP) was first proposed to distinctively adjust and refine the images by creating greater contrast of desired ASR crack features from the heavily textured background. Through a comprehensive parametric study, a suitable condition dark adjustment level applied to all three RBG layers of the images was obtained. It was evident that the proposed FEP successfully reduced CNN evaluation confusion and increased the classification accuracy from 90.90 % to 92.48 %. Next, the feature-adjusted images were further processed through three selected texture analysis algorithms, which aimed to further highlight and emphasise the ASR cracks. The investigated texture analysis techniques include morphology in the form of image erosion, local range filtering, and adaptive thresholding. Accordingly, it was demonstrated that the performance of the InceptionV3 model has been successfully boosted to an impressive validation accuracy of 94.07 % simply by integrating texture morphology with the developed FEP.

In summary, through the use of InceptionV3 and suitable feature adjustment incorporating texture morphology techniques, a successful two-stage procedure for evaluating ASR cracking has been established and powered by AI deep learning technology. One notable merit of the developed method is its ability in performing the assessment from the images without any requirement of surface treatment on the structures. This will open a new era of developing quick, smart, and cost-effective condition assessment tools to support the owners and managers of civil public works assets and other constructed infrastructures.

Declaration of Competing Interest

The authors declare that they have no known competing financial interests or personal relationships that could have appeared to influence the work reported in this paper.

Acknowledgment

The authors wish to thank the Deputy Director-general (Infrastructure Management and Delivery) of Department of Transport and Main Roads and the delegate in January 2021 for permissions to extract and use ASR inspection photos from the database of Queensland bridges.

References

[1] Abbass H. What is Artificial Intelligence? IEEE Transactions on Artificial Intelligence 2021;2(2):94–5.
[2] Abdo M. Structural health monitoring, history, applications and future. Open Science: A review book; 2014.
[3] Ai L, Soltangharaei V, Ziehl PJNE, Design.. Evaluation of ASR in concrete using acoustic emission and deep learning 2021;380:111328.
[4] Allahyari H, Heidarpour A, Shayan A, Nguyen VPJC, Composites C. A robust time-dependent model of alkali-silica reaction at different temperatures 2020;106:103460.
[5] Babich N. What Is Computer Vision; How Does it Work? Adobe Ideas, July: An Introduction; 2020. p. 28.
[6] Bajcsy P, Feldman S, Majurski M, Snyder K, Brady MJJ, o. m.. Approaches to training multiclass semantic image segmentation of damage in concrete 2020;279(2):98–113.
[7] Bezerra A. The Use of Artificial Intelligence for Assessing Damage in Concrete Affected by Alkali-Silica Reaction (ASR). Université d'Ottawa/University of Ottawa]; 2021.
[8] Bisong E. Building machine learning and deep learning models on Google cloud platform: A comprehensive guide for beginners. Apress; 2019.
[9] Bottou L. From machine learning to machine reasoning: An essay. J Mach Learn Res 2013;14:3207–60.

[10] Cha YJ, Choi W, Büyüköztürk OJCAC, Engineering I. Deep learning-based crack damage detection using convolutional neural networks 2017;32(5):361–78.
[11] Dorafshan S, Thomas RJ, Maguire MJC, Materials B. Comparison of deep convolutional neural networks and edge detectors for image-based crack detection in concrete 2018;186:1031–45.
[12] Fanijo EO, Kolawole JT, Almakrab AJCS, i. C. M.. Alkali-silica reaction (ASR) in concrete structures: Mechanisms, effects and evaluation test methods adopted in the United States 2021;15:e00563.
[13] Farnam Y, Geiker MR, Bentz D, Weiss J. Acoustic emission waveform characterization of crack origin and mode in fractured and ASR damaged concrete. Cem Concr Compos 2015;60:135–45.
[14] Feng D, Feng MQ. Computer vision for SHM of civil infrastructure: From dynamic response measurement to damage detection–A review. Eng Struct 2018;156:105–17.
[16] Gao Y, Mosalam KM. Deep transfer learning for image-based structural damage recognition. Comput Aided Civ Inf Eng 2018;33(9):748–68.
[17] Giada S, De Groeve T, Ehrlich D, Soille P. Information extraction from very high resolution satellite imagery over Lukole refugee camp. Tanzania *International Journal of Remote Sensing* 2003;24(22):4251–66.
[18] Godart, B., de Rooij, M. R., & Wood, J. G. (2013). *Guide to diagnosis and appraisal of AAR damage to concrete in structures*. Springer.
[19] Kurmi, Y., Chaurasia, V., & Kapoor, N. (2020). Design of a histopathology image segmentation algorithm for CAD of cancer. *Optik*, *218*, 164636.
[20] LeCun Y, Bengio Y, Hinton G. Deep learning *nature* 2015;521(7553):436–44.
[21] Leemann A. Raman microscopy of alkali-silica reaction (ASR) products formed in concrete. Cem Concr Res 2017;102:41–7.
[22] Luke JJ, Joseph R, Balaji M. Impact of image size on accuracy and generalization of convolutional neural networks. In: International Journal of Research and Analytical Reviews (IJRAR) 2019.
[23] Nguyen A, Chianese RR, Gharehbaghi VR, Perera R, Low T, Aravinthan T, et al. Robustness of deep transfer learning-based crack detection against uncertainty in hyperparameter tuning and input data. In: Hong Guan THTC, Li J, editors. Recent Advances in Structural Health Monitoring Research in Australia. Nova Science Publishers; 2022.
[24] Oey, T., Vehmas, T., Torkki, A., Ferreira, R. M., & Bohner, E. J. R. p. d. e. d. e. (2021). Predicting the incidence of alkali-aggregate reaction in Finnish bridges with machine learning. (15), 65-76.
[25] Roy, P., Dutta, S., Dey, N., Dey, G., Chakraborty, S., & Ray, R. (2014). Adaptive thresholding: A comparative study. 2014 International conference on control, Instrumentation, communication and Computational Technologies (ICCICCT).
[26] Saouma VE. Diagnosis & prognosis of AAR affected structures: state-of-the-art report of the RILEM Technical Committee 259-ISR, Vol. 31. Springer Nature; 2020.
[27] Schmidhuber J. Deep learning in neural networks: An overview. Neural Netw 2015;61:85–117.
[28] Shayan A, Xu A, Chirgwin G, Morris H. Effects of seawater on AAR expansion of concrete. Cem Concr Res 2010;40(4):563–8.
[29] Silva WRL, d., & Lucena, D. S. d.. Concrete cracks detection based on deep learning image classification. Proceedings; 2018.
[30] Soille P. Morphological texture analysis: an introduction. In: Morphology of condensed matter. Springer; 2002. p. 215–37.
[31] Spencer Jr BF, Hoskere V, Narazaki Y. Advances in computer vision-based civil infrastructure inspection and monitoring. Engineering 2019;5(2):199–222.
[32] Tayfur S, Yüksel C, Alver N, Akar O, Andiç-Çakır Ö. Evaluation of alkali–silica reaction damage in concrete by using acoustic emission signal features and damage rating index: Damage monitoring on concrete prisms. Mater Struct 2021;54(4):1–17.
[33] Thomas, M. D., Fournier, B., & Folliard, K. J. (2013). *Alkali-aggregate reactivity (AAR) facts book*.
[34] Thomas, M. D., Fournier, B., Folliard, K. J., & Resendez, Y. (2011). *Alkali-silica reactivity field identification handbook*.
[35] Uwanuakwa, I. D., Idoko, J. B., Mbadike, E., Reşatoğlu, R., & Alaneme, G. (2022). Application of deep learning in structural health management of concrete structures. Proceedings of the Institution of Civil Engineers-Bridge Engineering.
[36] Zahedi, A., Trottier, C., Sanchez, L. F., & Noël, M. (2021). Microscopic assessment of ASR-affected concrete under confinement conditions. *Cement and Concrete Research*, *145*, 106456.
[37] Ziehl P, ElBatanouny M. Low-level acoustic emission (AE) in the long-term monitoring of concrete. In: Acoustic Emission and Related Non-Destructive Evaluation Techniques in the Fracture Mechanics of Concrete. Elsevier; 2015. p. 217–36.

Further reading

[15] Fernandes I, Broekmans MAJM, Microstructure, & Analysis.. Alkali–silica reactions: an overview. Part I 2013;2:257–67.